

## Research Article

# Numerical Investigation on Rock-Fracturing Mechanism by Using Splitter under Hole Assistance

Hongsheng Li<sup>1,2</sup>, Songyong Liu<sup>1,2</sup>, Gang Cheng<sup>1,2</sup>, and Chuwen Guo<sup>1,3</sup>

<sup>1</sup>School of Mechatronic Engineering, China University of Mining and Technology, Xuzhou 221116, China

<sup>2</sup>Jiangsu Collaborative Innovation Center of Intelligent Mining Equipment, China University of Mining and Technology, Xuzhou 221008, China

<sup>3</sup>School of Electric Power Engineering, China University of Mining and Technology, Xuzhou 221116, China

Correspondence should be addressed to Songyong Liu; lsycumt@163.com

Received 26 February 2019; Revised 21 June 2019; Accepted 22 July 2019; Published 16 September 2019

Academic Editor: Marco Lepidi

Copyright © 2019 Hongsheng Li et al. This is an open access article distributed under the Creative Commons Attribution License, which permits unrestricted use, distribution, and reproduction in any medium, provided the original work is properly cited.

In this work, a numerical model of rock breaking under hole assistance was established based on the finite element method (FEM) coupling with smoothed particle hydrodynamics (SPH) to reveal rock-breaking mechanisms and analyze the reasons for crack formation and propagation under hole assistance. In addition, the numerical model was verified by experiment with and without a hole, and the simulation results are basically consistent with the experimental results in rock breaking. During the process of rock fracturing, the hydraulic splitter was first inserted into the predrilling hole, and then the wedges were pushed into the rock under the action of the hydraulic pressure. In this process, the splitter wedge was separated from the two sides, and the transverse bursting force was transmitted to the rock. Finally, the main fracture formed and the rock mass broke due to the bursting force. The results show that the cracks propagate along the approximately straight lines  $OO_1$  (the distance between the auxiliary holes and the left predrilled fracturing hole) and  $OO_2$  (the distance between the auxiliary holes and the right predrilled fracturing hole) before extending to the auxiliary hole which is unlike the crack propagation in rock without auxiliary holes, and the crack propagating direction gradually approaches horizontally and is vertical to the side after passing through the auxiliary holes. Moreover, when the auxiliary holes are located at the prefabricated angles  $\alpha = 40^\circ$  and  $45^\circ$ , the crack propagation can be well induced and the cracks pass through the auxiliary holes. However, at  $\alpha = 50^\circ$ , the auxiliary holes can no longer well induce the crack propagation in the process of rock breaking; however, the fracturing pressure is still less than that with no auxiliary holes, indicating that the auxiliary holes play a positive role in guiding rock breaking.

## 1. Introduction

In China, the annual amount of rock roadway excavation is much greater than 2000 km, and the production of roadways accounts for 15% to 25% of total projects [1]. However, due to restriction of construction equipment, the extent of rock roadway is only around 60 m per month, which seriously restricts the coordinated development of coal mine production. For hard rock with a hardness coefficient  $f \geq 10$ , regardless of the use of a full-face tunnel boring machine or roadheader, the impact and friction of the pick is increases, and the working environment of the roadheader is worse, reducing the effectiveness of the tunneling machine and increasing the cost of a hard rock roadway [2, 3]. Thus, a new

method of rock breaking using a hydraulic splitter is proposed to solve this problem. And it has the advantages of safety, high efficiency, low cost, and so on (Figure 1).

In order to study the rock crack propagation and rock-breaking mechanism under the action of hydraulic splitter, the microfailure analysis of rocks was carried out, as shown in Figure 2. When the wedge block was intruded into a rock mass, the compressed part of the rock showed crushing or plastic deformation to form a dense core. During the whole process of rock breaking, the relationship between the wedge depth and hydraulic pressure was not corresponding to each other, but a sudden step breaking occurred at a certain critical value under the action of complex tensile or shear stresses. At this time, the natural microcracks were partly

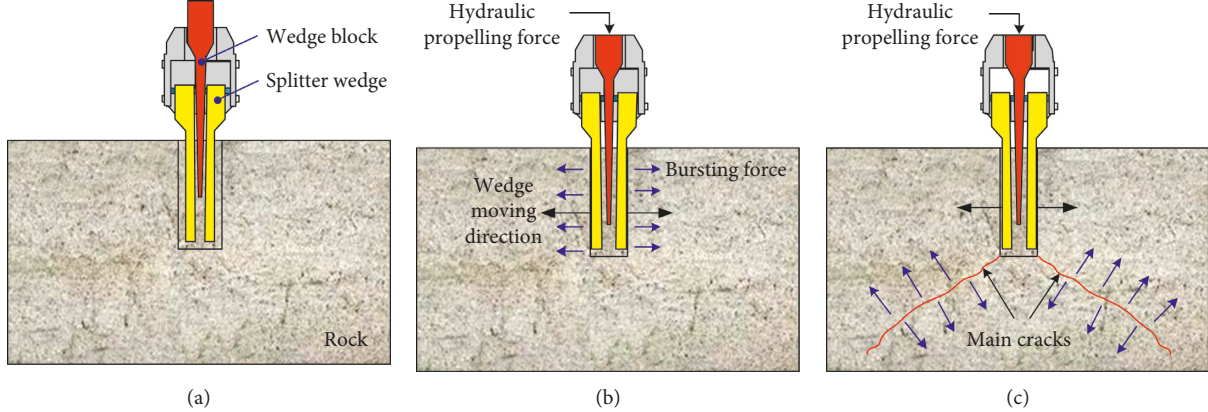


FIGURE 1: Rock-breaking process using hydraulic splitter: (a) insertion of hydraulic splitter; (b) hydraulic propelling action; (c) rock fracturing.

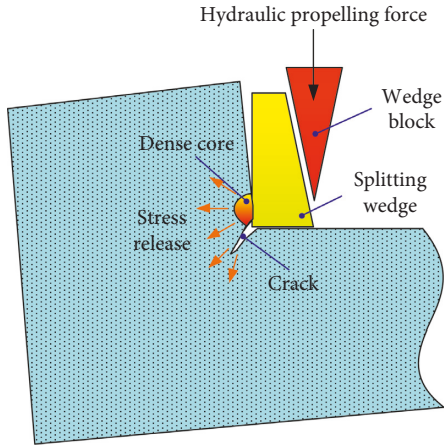


FIGURE 2: Microcosmic process of rock breaking.

tensioned and partly compressed. With the further increase of the splitting force on the dense core, the rock on both sides of the compacted core will break down and the main crack in the rock will continue to expand. The wedge will continue to invade the rock, leading to the load in the crushed area to rise again, and the penetration depth and hydraulic pressure will return to a certain proportion.

The rock-failure mechanism during the process of rock breaking is more complicated. There are several classical models on the crack propagation, such as the Griffith criterion, two-dimensional (2D) crack slip model, and blunt crack zone model. The initiation and propagation of a fracture from a single Griffith crack in a biaxial compressive stress field were studied [4], and the result indicated that Griffith's theory of brittle fracture offers a reliable prediction of the fracture initiation stress. The 2D crack slip model was first proposed in [5], and the flexural tensile crack generated by the end of the sliding fracture is considered to be the main mechanism of the new crack generation under the pressure shear load. Bazant and Cedolin utilized the blunt crack approach for simulating concrete cracking [6], assuming the modulus of elasticity is zero in the direction perpendicular to the crack surface, but nonzero

elastic modulus remains parallel to the crack surface direction. The rock-soil mechanical model considering the strain softening phenomenon and the Rayleigh damping based on the Mohr-Coulomb strength theory was established [7, 8] to simulate the impact drilling process and reveal the mechanism of tensile aging, compression failure, and fatigue failure. A generic model for predicting hydraulic fracture initiation from arbitrarily oriented wellbores was developed, and the model was applied in a series of in situ stress conditions to study the effect of wellbore orientation on fracture initiation using nondimensional parameters [9]. Considering the influence of the casing, analytical solutions for stress distribution around a cased wellbore were derived, based on which a prediction model for hydraulic fracture initiation with the oriented perforation technique was established [10].

In numerical simulation research, a three-dimensional (3D) finite element model was established by Guangqing and Mian [11] to study the factors that influence the fracture shape in orientated hydraulic fracturing based on rock mechanical tests and practical data interpretation. To analyze the initiation and propagation mechanism of a crack, the principle of gas seepage in cracks and the hydraulic fracturing process were analyzed synthetically through numerical simulation [12], the results of which showed that the rock stress state greatly affects the crack propagation and the crack propagated randomly with bifurcation when the two ground stresses on the horizontal plane were equal. The influences of various complex factors, such as geostress, rock mechanic characteristics, and fracturing fluid characteristics, on hydraulic fracturing expansion were investigated [13], and the initiation pressure, maximum crack width, and crack propagation length were obtained under different maximum horizontal stress conditions. A 3D distinct element code was used and developed to simulate the initiation and propagation of hydraulically induced fractures in a typical reservoir hosted by a rock mass [14], and the analysis results confirmed the previous understanding that the success of the hydraulic fracturing process not only depends on controllable parameters such as fracture fluid properties

and injection rate but also relies on the uncontrollable parameters. The geomechanical responses during hydraulic fracturing operations for generalized Marcellus shale gas reservoirs were also numerically investigated [15], and the result showed that hydraulic fracturing produced stable fracture propagations and that the high effective shear stress was concentrated near the fracture tip. Ingraffea and Heuze [16] proposed a finite element model for the prediction of discrete fracture propagation in rock structures loaded in compression, and they found that the model accurately predicted both stable and unstable fracture propagations observed experimentally. The effect of anisotropy on the hydraulic fracture initiation pressure was investigated by establishing an analytical model of the stresses around wellbore in shale gas reservoirs, in consideration of stratum dip direction, dip angle, and in situ stress azimuth [17].

From experiments, the prediction models of rock mechanics parameters were established to increase the rate of penetration and to reduce cost, and the rock-breaking mechanism of complex formation of cone and PDC bit was studied [18]. In addition, according to the properties of the rock mechanics and the bit applications of adjacent wells, structures, such as tooth type, crown probe, tooth assembly parameters, and the hydraulic structure of selected bits, were optimized [19]. The relationship between the water pressure and the 3D stress at the crack tip during crack propagation was commonly obtained by triaxial fracturing tests of the rock mass. The relation among reopening pressure, in situ stresses, and the injection flow rate was clarified experimentally [20], and a transverse crack was induced perpendicular to a borehole axis in hydraulic fracturing stress measurements. To model the mechanism of the shear failure, a row of suitably oriented model flaws was considered and the elasticity boundary value problem associated with the out-of-plane crack growth from the tips of the flaws was solved [21]. The result indicated that for a certain overall orientation of the flaws, the growth of the out-of-plane cracks may become unstable, leading to possible macroscopic faulting. In addition, the mechanism of the axial splitting under the uniaxial compression condition was realized through the connection and penetration of the smaller prestored fissure in the shear zone [22–24]. A mechanism of open hole instability was considered based on the growth of preexisting microfractures in the direction of the greatest compression [25], and the major factor enabling the preexisting 3D cracks to propagate extensively was the presence of the intermediate principal compression near the opening wall. To provide information on the formation of fractures around deep-level mine tunnels under controlled conditions, a series of physical and numerical model tests were performed to investigate the rock behavior surrounding circular excavations under high confining pressures, which can provide confidence for the application of the numerical model to the design of mine tunnels at great depths [26]. In order to investigate the effect of different perforation angles on the fracture initiation and propagation during hydraulic fracturing of highly deviated well in oil and gas saturated formation, laboratory experiments of the hydraulic fracturing

was carried out by Zhu et al. [27]. Moreover, a calcite-filled fracture from outcrops of Wufeng-Longmaxi shale was performed experimentally to study the propagation mechanism of fractures during hydraulic fracturing [28].

The achievements of the previous studies provide a reference for this paper, but there still exists room for improvement. However, the existing research only focuses on the influence of spacing and size of hole on the stress distribution without hole assistance. The rock-fracturing mechanism using a hydraulic splitter under hole assistance is complex and poorly understood; this lack of understanding has limited the wider application of hydraulic splitters as rock-breaking tools. Therefore, a theoretical analysis of rock breaking containing hole is firstly made, and then a numerical model of rock breaking under hole assistance is established, with the aim of revealing the rock-breaking mechanism and explaining the reasons for crack formation, including the crack initiation and propagation. Finally, the fracturing pressure and crack propagations with different prefabricated angles are investigated to obtain appropriate auxiliary hole positions for guiding rock breaking.

## 2. Theoretical Analysis of Rock Breaking Containing Hole

The mechanical properties of the rock samples with holes were weakened to a certain extent in the elastic modulus, and the compressive strengths were compared with the original rock samples. In addition, the stress distribution around the holes was changed. Assuming there is a hole in the infinite rock sample [9, 10, 17], the mechanical model of the stress distribution around the hole is as shown in Figure 3.

Based on the theory of elasticity, the stress field at any point around the hole can be expressed as

$$\left\{ \begin{array}{l} \sigma_b = \left( 1 - \frac{a^2}{b^2} \right) \frac{q}{2} + \left( 1 - \frac{4a^2}{b^2} + \frac{3a^4}{b^4} \right) \frac{q}{2} \cos 2\theta, \\ \sigma_\theta = \left( 1 + \frac{a^2}{b^2} \right) \frac{q}{2} - \left( 1 + \frac{3a^4}{b^4} \right) \frac{q}{2} \cos 2\theta, \\ \tau_{b\theta} = - \left( 1 + \frac{2a^2}{b^2} - \frac{3a^4}{b^4} \right) \frac{q}{2} \sin 2\theta, \end{array} \right. \quad (1)$$

where  $\sigma_b$  is the radial principal stress component of rock,  $\sigma_\theta$  is the principal stress component of the rock ring direction,  $\tau_{b\theta}$  is the shear stress component of rock,  $q$  is the uniform unidirectional tensile force of rock,  $a$  is the radius of the hole in the rock,  $b$  is the distance from an empty hole at any point in the rock, and  $\theta$  is the angle between the connection of any point in the rock and the center of the hole and the  $x$ -axis. When any point on the rock sample falls on the circumference of the empty hole ( $b = a$ ), the hoop principal stress can be expressed as

$$\sigma_\theta = q(1 - 2 \cos 2\theta). \quad (2)$$

In this case, the hoop principal stress varies with the change of  $\theta$ . The ratio of the maximum hoop principal stress

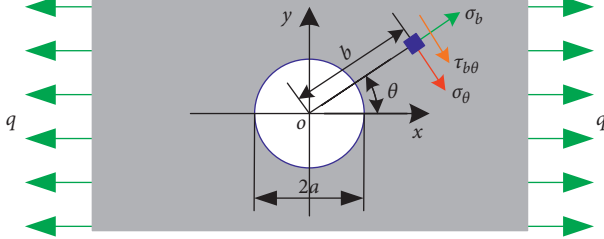


FIGURE 3: Mechanical model of stress distribution around a hole in the infinite rock mass.

around the holes to that with none is defined as the stress concentration coefficient  $K_\sigma = (\sigma_\theta)_{\max}/q$ , calculated as 3 for that of the hole. According to equation (2), the variation of the hoop principal stress component with  $b$  along the  $x$ -axis and the  $y$ -axis is shown in Figure 4. The value of the circumferential stress component at several specific distances along the  $y$ -axis coordinate system is shown in Table 1. When  $b = 5a$ , the increase of the principal stress component along the  $y$ -axis is only 2% comparatively. This indicates that the stress concentration phenomenon around holes is local, and the effective concentration range is approximately 5 times the diameter.

The above analysis shows that the rock is subjected to a uniform uniaxial tensile force. The stress field superposition model when the rock is subjected to 2D uniform stress is shown in Figure 5.

By substituting  $q = q_1$  and  $q = q_2$  and  $\theta = \theta + \pi/2$  into equation (1), an expression for the stress distribution around holes in the rock under uniform tensile stress  $q_1$  and  $q_2$  in the  $x$ - and  $y$ -directions can be obtained, and then two uniform tensile directions can be synthesized from them. The expression of the stress distribution is

$$\left\{ \begin{array}{l} \sigma_b = \left(1 - \frac{a^2}{b^2}\right) \frac{q_1 + q_2}{2} + \left(1 - \frac{4a^2}{b^2} + \frac{3a^4}{b^4}\right) \frac{q_1 - q_2}{2} \cos 2\theta, \\ \sigma_\theta = \left(1 + \frac{a^2}{b^2}\right) \frac{q_1 + q_2}{2} - \left(1 + \frac{3a^4}{b^4}\right) \frac{q_1 - q_2}{2} \cos 2\theta, \\ \tau_{b\theta} = -\left(1 + \frac{2a^2}{b^2} - \frac{3a^4}{b^4}\right) \frac{q_1 - q_2}{2} \sin 2\theta. \end{array} \right. \quad (3)$$

When  $q_1 = q_2 = q$ , equation (3) can be simplified as

$$\left\{ \begin{array}{l} \sigma_b = \left(1 - \frac{a^2}{b^2}\right) q, \\ \sigma_\theta = \left(1 + \frac{a^2}{b^2}\right) q, \\ \tau_{b\theta} = 0. \end{array} \right. \quad (4)$$

There is obvious stress concentration phenomenon in the round hole, with a concentration coefficient of 2. Therefore,

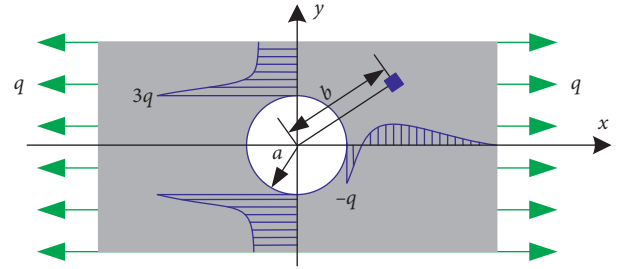


FIGURE 4: Hoop principal stress variation tendency with  $b$ .

TABLE 1: Hoop principal stress of  $y$ -axis at several specific distances.

$b$	$a$	$2a$	$3a$	$4a$	$5a$
$\sigma_\theta$	$3q$	$1.22q$	$1.07q$	$1.04q$	$1.02q$

the rock-containing hole is conducive to the expansion of rock cracks, which further aggravates the stress concentration and breaks the whole rock.

### 3. Methodology

**3.1. Geometric Model and Boundaries.** The geometric model and numerical model of rock breaking by the splitter was set up as shown in Figures 6(a) and 6(b). The splitter wedges were simplified as two  $\varphi 45$  mm  $\times$  350 mm semicircular with 2 mm/s velocity. Similarly, the rock was also simplified as 800 mm  $\times$  800 mm  $\times$  600 mm cuboid. In addition, a pre-drilled fracturing hole and two auxiliary holes with  $\varphi 45$  mm  $\times$  350 mm were on the top of the rock, and the angle was 40°. Because the effective stress concentration range of the holes was 5 times the diameter, the distance between the auxiliary holes and the predrilled fracturing holes was set as 170 mm. To avoid the effect of a boundary and rock size on rock breaking, the rock bottom and sides were all set as no-reflection boundaries [29, 30]. The rock comprises 381518 particles with a uniform distribution, and the particle size was equal to 1.0 mm. Automatic Lagrange/Lagrange coupling was adopted to manage the interaction problem between wedges and rock [31]. Considering the working environment with the confining pressure, two steel plates were established on the basis of the  $z$ -axis of the rock, and the uniform pressure of 2 MPa was fixed to the steel plate, as shown in Figure 6(c). The numerical model in this paper adopted the above-described geometric model, mesh model, and boundary conditions unless otherwise stated.

**3.2. Modeling of the Rock Material [2].** To study the stress field and dynamic fracture of a rock specimen, the Johnson–Holmquist constitutive model (JH2) is used. This model was originally formulated for a description of the brittle response of ceramics and has also been widely used to simulate the dynamic behavior of brittle or quasibrittle materials, such as rock, concrete, glass, and ice [32–35].

**3.2.1. Equation of State for Rock [2].** The polynomial equation of state (EOS), which is commonly used with the

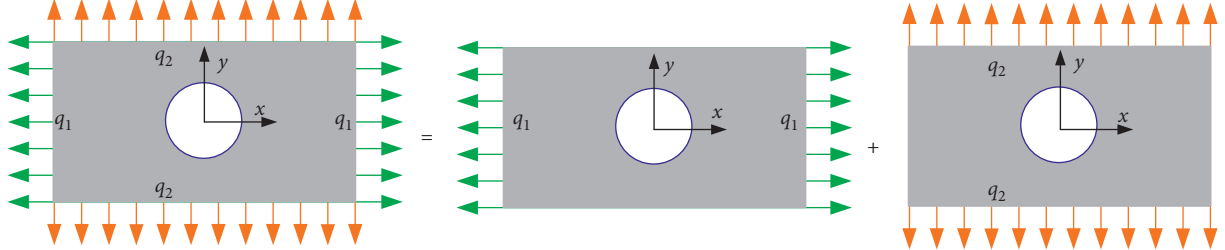


FIGURE 5: Superposition model of stress field under two directions of uniform tension.

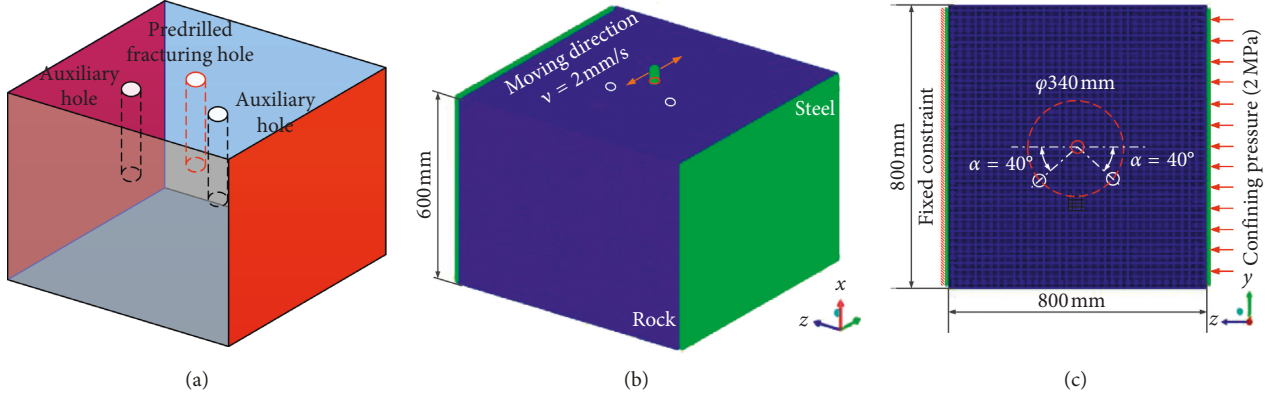


FIGURE 6: (a) Geometric model; (b) numerical model; (c) boundary conditions.

JH2 model, was used for the rock specimen. The relationship between hydrostatic pressure  $P$  and volumetric strain  $\mu$  for the polynomial EOS in the Johnson–Holmquist model is shown in Figure 7.

Here,  $\mu = (\rho/\rho_0) - 1$  is adopted to describe the compression status, where  $\rho_0$  is the reference density and  $\rho$  is the current density. An incremental pressure  $\Delta P$  is added to the calculated pressure from the polynomial EOS, and the  $\Delta P$  magnitude is determined based on the damage level the rock has experienced. When the maximum strength of the rock has been reached, the rock damage increases because the elastic distortion energy starts to decrease. The extra pressure  $\Delta P$  is caused by the conversion of distortion energy into potential hydrostatic energy accompanied by an increase in volumetric strain, in which the conversion amount is controlled by the fraction  $0 \leq \beta \leq 1$  [33, 36]. The polynomial EOS can be expressed as follows:

$$P = K_1\mu + K_2\mu^2 + K_3\mu^3 + \Delta P, \quad (5)$$

where  $K_1$ ,  $K_2$ , and  $K_3$  are the material parameters to be obtained from the experiments.

**3.2.2. JH2 Strength Model [2].** The JH2 model consists of the strength models of intact, damaged, and fractured materials. The strength of the intact materials follows the  $J_2$  material theory of plastic mechanics as follows:

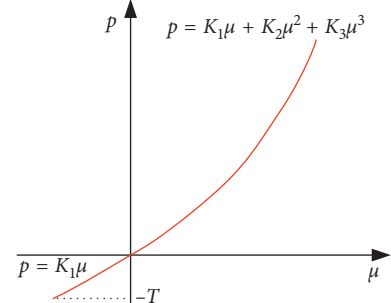


FIGURE 7: Relation between pressure and volumetric strain in JH2 model.

$$\begin{aligned} J_2 &= \frac{1}{2}S_{ij}S_{ij} = \frac{1}{6}\left[\left(\sigma_x - \sigma_y\right)^2 + \left(\sigma_y - \sigma_z\right)^2 + \left(\sigma_z - \sigma_x\right)^2\right] \\ &\quad + \tau_{xy}^2 + \tau_{yz}^2 + \tau_{zx}^2 = \frac{1}{6}\left[\left(\sigma_1 - \sigma_2\right)^2 + \left(\sigma_2 - \sigma_3\right)^2 \right. \\ &\quad \left. + \left(\sigma_3 - \sigma_1\right)^2\right], \end{aligned} \quad (6)$$

where  $J_2$  is the second invariant of the deviatoric stress tensor;  $S_{ij}$  are the components of the deviatoric stress tensor;  $\sigma_x$ ,  $\sigma_y$ , and  $\sigma_z$  are the normal components of the stress

tensor;  $\tau_{xy}$ ,  $\tau_{yz}$ , and  $\tau_{zx}$  are the shearing components of the stress tensor; and  $\sigma_1$ ,  $\sigma_2$ , and  $\sigma_3$  are the principal stresses.

The equivalent stress is commonly used for a description of the elastic limit of the failure criteria and is given as

$$\sigma = \sqrt{3J_2} = \sqrt{\frac{1}{2} [(\sigma_1 - \sigma_2)^2 + (\sigma_2 - \sigma_3)^2 + (\sigma_3 - \sigma_1)^2]}. \quad (7)$$

For intact material, the normalized strength is given by

$$\sigma_I^* = A(P^* + T^*)^N \cdot (1 + C \ln \dot{\varepsilon}^*), \quad (8)$$

where  $\sigma_I^* = \sigma_I/\sigma_{\text{HEL}}$  is the normalized equivalent strength,  $\sigma_I$  is the actual intact strength, and HEL is the Hugoniot elastic limit of the material, which indicates the elastic limit of the material at the turning point of the linear section of the free surface velocity curve [37]; in addition,  $P^* = P/P_{\text{HEL}}$  is the normalized pressure,  $P$  is the actual pressure,  $P_{\text{HEL}}$  is the pressure at the Hugoniot elastic limit,  $T^* = T/T_{\text{HEL}}$  is the normalized hydrostatic tensile limit (HTL) that material can withstand,  $\dot{\varepsilon}^* = \dot{\varepsilon}/\dot{\varepsilon}_0$  is the normalized strain rate,  $\dot{\varepsilon}$  is the actual equivalent strain rate,  $\dot{\varepsilon}_0 = 1.0 \text{ s}^{-1}$  is the reference strain rate, and  $A$ ,  $N$ , and  $C$  are the material parameters.

The equivalent strain rate can be given as

$$\dot{\varepsilon} = \sqrt{\frac{2}{9} [(\dot{\varepsilon}_x - \dot{\varepsilon}_y)^2 + (\dot{\varepsilon}_y - \dot{\varepsilon}_z)^2 + (\dot{\varepsilon}_z - \dot{\varepsilon}_x)^2 + \frac{3}{2} (\dot{\gamma}_{xy}^2 + \dot{\gamma}_{yz}^2 + \dot{\gamma}_{zx}^2)]}, \quad (9)$$

where  $\dot{\varepsilon}_x$ ,  $\dot{\varepsilon}_y$ , and  $\dot{\varepsilon}_z$  are the normal strain rates and  $\dot{\gamma}_{xy}$ ,  $\dot{\gamma}_{yz}$ , and  $\dot{\gamma}_{zx}$  are the shear strain rates.

As shown in Figure 8(a), if the current normalized equivalent stress becomes larger than the intact strength of the materials, it will return to the yield surface, and plastic deformation will take place. With an increase in the unrecoverable plastic deformation, the damage in the material will accumulate, and its strength will gradually decrease from intact strength  $\sigma_I^*$  to a lower state  $\sigma_D^*$ . The new yield surface then depends on the level of damage,  $0 \leq D \leq 1$ . If the material is completely damaged ( $D = 1$ ), the new yield surface will decrease to a fractured material surface.

For the fractured material, the normalized strength is represented as

$$\sigma_F^* = B(P^*)^M \cdot (1 + C \ln \dot{\varepsilon}^*), \quad (10)$$

where  $B$  and  $M$  are the parameters of the fractured material and  $P^*$ ,  $C$ , and  $\dot{\varepsilon}^*$  are the same as those in equation (8). An upper limit  $\sigma_{F\max}^*$  is used to control the position of the strength-fractured surface.

For the damaged material, the normalized strength relating closely to the damage can be given as

$$\sigma_D^* = \sigma_I^* - D(\sigma_I^* - \sigma_F^*). \quad (11)$$

**3.2.3. JH2 Failure Criterion [2].** In the JH2 model, the yield and failure surfaces coincide at any point in time. However, the amount of plastic strain required for changing the status of the material from intact to fracture depends on the local

pressure, as shown in Figure 8(b). The equivalent plastic strain to fracture for this model is obtained from

$$\varepsilon_p^f = D_1 (P^* + T^*)^{D_2}, \quad (12)$$

where  $D_{r1}$  and  $D_{r2}$  are two damage constants. The material cannot undertake any plastic strain at  $P^* = -T^*$ .

As the material undergoes plastic deformation, damage accumulates in the material, and its value can be calculated as

$$D = \sum \left( \frac{\Delta \varepsilon_p}{\varepsilon_p^f} \right), \quad (13)$$

where  $\Delta \varepsilon_p$  is the effective plastic strain during a cycle of integration. In the elastic region, no plastic deformation occurs, and the material remains intact with  $D = 0$ . The total equivalent plastic strain increases as the material undergoes permanent deformations owing to the large equivalent stresses. This reduces the material strength ( $0 \leq D \leq 1$ ). When the equivalent plastic strain becomes equal to the strain to fracture  $\varepsilon_p^f$ , the material is completely damaged, and its strength decreases to the fractured strength.

When the JH2 material model is applied to this numerical model of rock fragmentation by hydraulic splitter, the material constants should be provided. The typical material constants for rock specimen are listed in Table 2.

#### 4. Verification of the Numerical Model

The experiment also applies 2 MPa confining pressure to rocks to verify the simulation results. A drilled hole and two auxiliary holes with the same simulation model parameters will be firstly drilled on the top surface, and then the rock-breaking experiment using hydraulic splitter is carried out. In addition, the boundary conditions for simulation and experiment are identical.

**4.1. Experimental Equipment.** To accomplish the experiment of rock breaking, the rock-drilling platform and hydraulic splitter must be used, as shown in Figures 9 and 10, respectively.

The rock-drilling platform was used to reasonably arrange the drilling hole layout, and then the hydraulic splitter was used for rock breaking in the drilling hole. The rock-drilling platform mainly comprises a drilling system, hydraulic system, and measurement system. The drilling system includes a lifting platform, supporting frame, hydraulic rock drill, propulsion cylinder, propulsion guide, and guide frame. The lifting platform and rear support frame were mainly used to adjust the vertical displacement and fix the oil cylinder, support the propelling oil cylinder and stabilize the testbed, and advance the guide rail for the working track of the hydraulic rock drill.

The experimental device of the hydraulic splitter system, as shown in Figure 10, is mainly composed of a high-pressure plunger pump, airborne engine, manual direction valve, overflow valve, and spillover. High-pressure hydraulic oil is output from the high-pressure pumping station to split

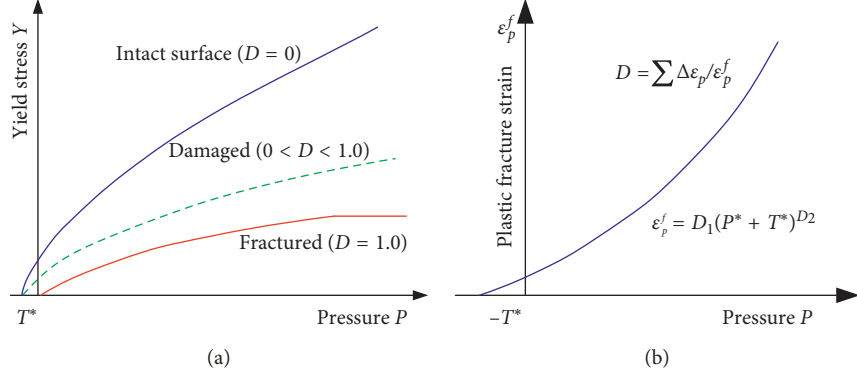


FIGURE 8: Equivalent strength and plastic strain versus pressure. (a) Strength model. (b) Damage model.

TABLE 2: Rock mechanical parameters of JH2 model.

Parameter	Value
Reference density $\rho_0$	2630 kg/m <sup>3</sup>
Uniaxial compressive strength $\sigma_c$	122.2 MPa
Uniaxial tensile strength $\sigma_t$	9.5 MPa
Poisson's ratio $\nu$	0.30
Intact rock bulk modulus $K$	25.7 GPa
Intact rock shear modulus $G$	16.9 GPa
<i>Strength constants</i>	
Hugoniot elastic limit (HEL)	4.5 GPa
Intact strength constant $A$	1.01
Intact strength exponent $N$	0.83
Strain rate coefficient $C$	0.005
Fractured strength constant $B$	0.65
Fractured strength exponent $M$	0.72
Max fractured strength ratio $\sigma_{F\max}^*$	0.5
<i>Pressure constants</i>	
Intact rock bulk modulus $K_1$	25.6 GPa
Polynomial EOS constant $K_2$	-4500 GPa
Polynomial EOS constant $K_3$	3e5 GPa
<i>Failure constants</i>	
Hydro tensile limit (HTL)	-54 MPa
Damage constant $D_1$	0.005
Damage constant $D_2$	0.7
Bulking factor $\beta$	0.5
Type of tensile failure	Hydro

the wedge. The pressure sensor connects to the pipeline through three pipes, and the fracturing pressure can be collected and output to a laptop. The displacement sensor is fixed on the splitter to obtain the bursting velocity of the hydraulic splitter.

In addition, the hydraulic splitter is based on the high-pressure hydraulic oil produced by a diesel engine power station as the energy source. The energy source is transported to the cylinder pipes of each splitter through oil pipes, and the splitting force can reach hundreds, or even thousands, of tons. Thus, the rock can be easily split up based on the characteristic that the rock tensile strength is far less than the compressive strength. The hydraulic splitter is first inserted into the predrilling hole, and then the wedges are pushed into the rock under the action of the hydraulic pressure. In this process, the split wedge is separated from the two sides, and the transverse bursting

force is transmitted to the rock. Finally, the main fracture is formed and the rock mass breaks under the action of the bursting force. The related parameters of the rock-splitting system are shown in Table 3.

#### 4.2. Comparison of Experimental and Numerical Results

**4.2.1. Contrast Verification of Rock-Breaking State.** To validate the rock-breaking model, a comparison of the rock-breaking state was made between the experimental and numerical results with and without auxiliary holes. From the simulation and experimental results without auxiliary holes, four crack propagations existed on the upper surface of the rock. The rock fracture along the main crack occurred and divided into two parts. The crack mainly propagated along the angle of about 30° in the horizontal direction and then tended to penetrate the rock horizontally, resulting in the whole fracture, as shown in Figures 11(a) and 11(b). Therefore, the holes will be prefabricated near the original crack propagation angle of 30° to obtain the appropriate hole-assisted angle.

In this paper, a prefabricated hole with angles of  $\alpha = 40^\circ$ ,  $45^\circ$ , and  $50^\circ$  was used to study the effect of auxiliary holes on directional fracture. According to the simulation results of rock breaking with hole assistance, the corresponding experiment was carried out. Firstly, the rock was drilled according to the simulation research model, and the angle among the  $OO_1$ ,  $OO_2$ , and horizontal directions was 40°. The diameters and depths of the auxiliary holes and predrilled fracturing hole were all 45 mm and 350 mm, respectively. The distance between the auxiliary holes and the predrilled fracturing hole ( $OO_1$ ) was 170 mm, as shown in Figure 11(c). The confining pressure was set to 2 MPa, identical to the simulation condition, and the left side of the rock was fixed while the right side was loaded with the confining pressure.

The rock-breaking state using a hydraulic splitter is shown in Figure 11(d). The rock-breaking crack propagated from the predrilled fracturing hole circumference to the auxiliary hole and, after passing through the auxiliary hole, tended to penetrate the whole rock side and break it. The angles between the cracks on the left and right sides of the rock and the straight line in the horizontal direction were approximately 36° and 30°, respectively. Compared with the design angle of

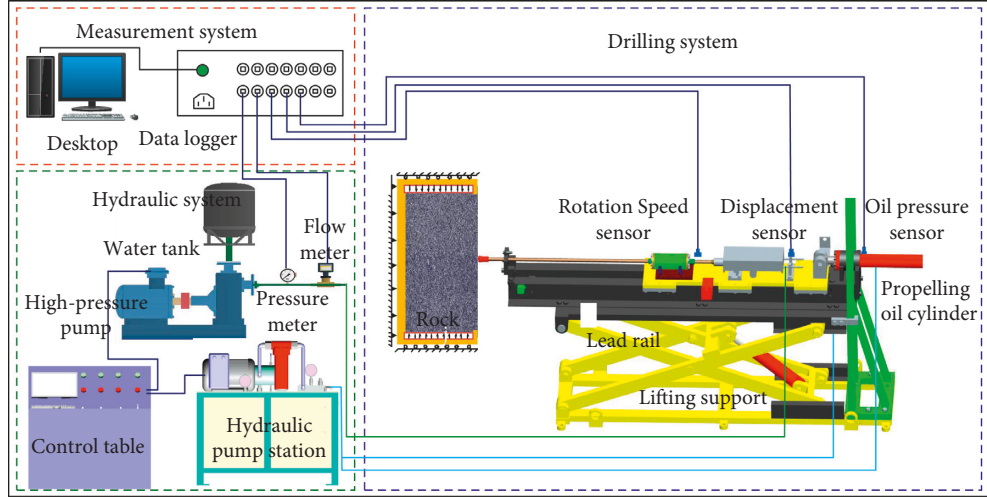


FIGURE 9: Experimental platform for rock drilling.

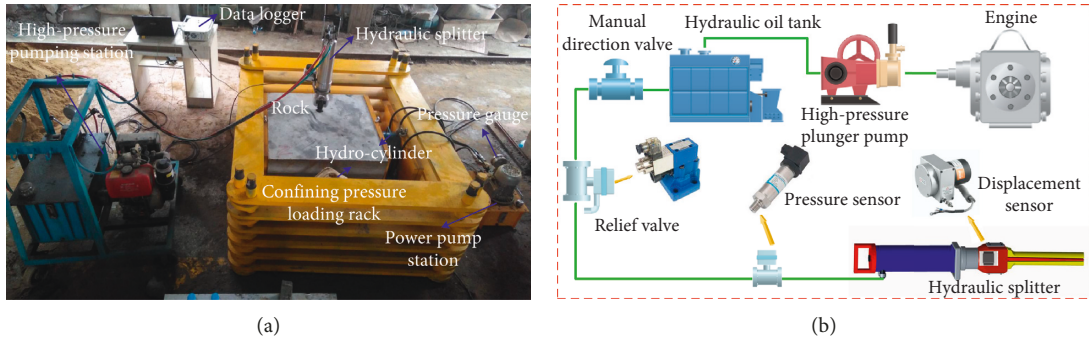


FIGURE 10: Experimental device and principle diagram of rock splitting.

$40^\circ$ , the maximum deflection angle was only  $6^\circ$ . Although the propagation path deviates from the angle of crack propagation, the crack propagation passes through the auxiliary holes, indicating that the auxiliary holes can effectively induce crack propagation, but the angle between the crack propagation and the horizontal line cannot be completely coincided due to the inhomogeneity of the rock itself. Moreover, the crack propagation path and rock-breaking state of the experiment agree with the simulation results, comparing Figures 11(d) and 14(d), which indicates that the simulation was validated well by the experiments.

**4.2.2. Comparison Verification of Fracturing Pressure.** Figure 12 presents the simulation and experimental fracturing pressure under hole assistance at  $\alpha = 40^\circ$ . During the process of rock breaking, the fracturing pressure curve experienced a short decline and then continued to rise. This corresponds to the phenomenon of wave suspension in the simulation, indicating that the crack was induced. That is, when the crack extended to the auxiliary hole, the fracturing pressure briefly decreased and then continued to rise.

It can be seen from Figure 12 that the simulation and experimental fracturing pressures increase first and then

decrease slightly. After this, they rise sharply to the maximum value and then decrease sharply to the stable value. When the crack propagates to the auxiliary holes, it is not enough to break the rock when the tensile stress is released immediately after the fracture crack reaches the auxiliary holes, and the splitter wedge must continue to separate a certain distance before the tensile stress reaches the level of sufficient crack propagation; thus, the fracturing pressure appears to stagnate. Then, the fracturing pressure increases sharply again; when the fracturing pressure reached its peak, the crack diffused until the whole rock was broken. After rock breaking, the fracturing pressure slowed sharply and tended to be stable. The simulation and experimental fracturing pressure curves show the same trends, and the peak values of the fracturing pressures are 35.1 MPa and 39.9 MPa, respectively, with a relative error of 12%, indicating that the simulation is feasible.

## 5. Results and Discussion

Figure 13 shows the equivalent effective stress nephogram of the auxiliary hole-assisted fracturing process. Firstly, it can be seen from Figure 13(a) that when the wedge begins to separate and contact the rock, the compressive stress is distributed on both sides of the borehole circumference in

TABLE 3: Related parameters of the rock-splitting system.

Power type	Engine power	Working pressure	Flow rate	Wedge length	Borehole depth	Borehole diameter	Theoretical splitting force
Diesel type	5.5 kW	60 MPa	4 L/min	150 mm	$\geq 350$ mm	$\geq \varphi 42$ mm	800 ton

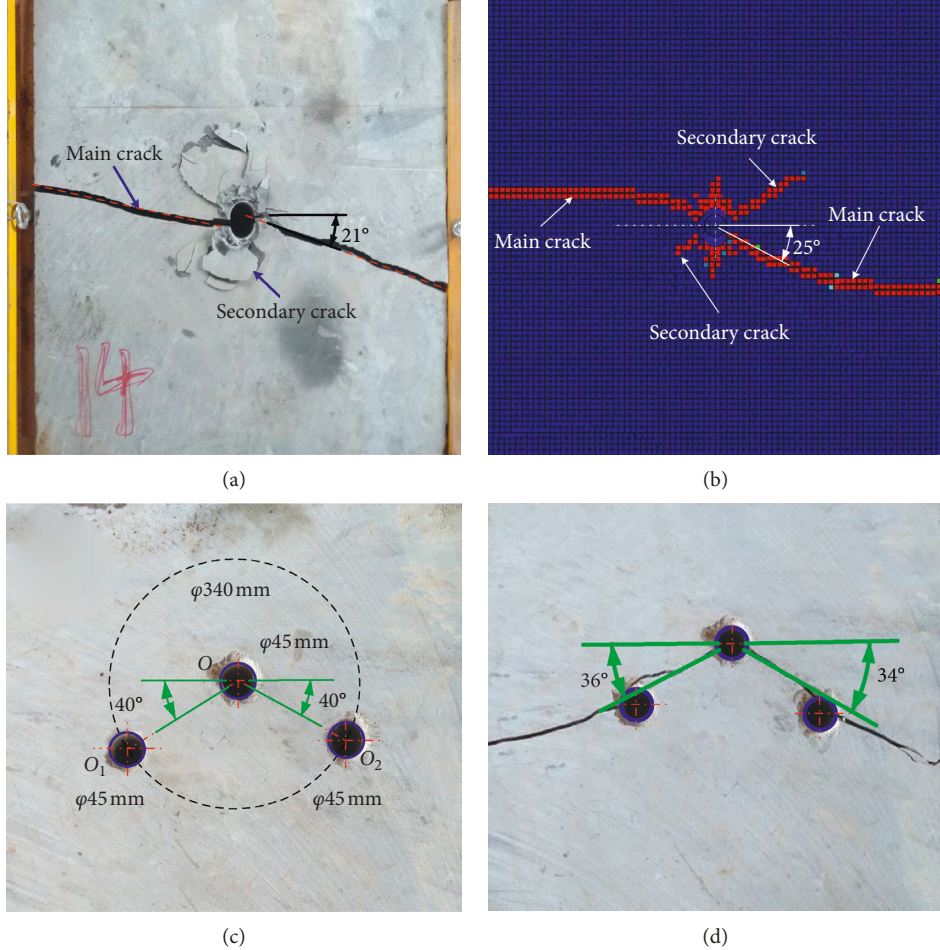


FIGURE 11: Rock-breaking state with nonauxiliary holes for (a) experiments and (b) simulation; (c) parameters of hole-assisted rock breaking; (d) experimental rock-breaking state with auxiliary hole.

the direction of the wedge separation, and the tensile stress is concentrated on the left and right sides of the borehole circumference.

Figure 13(b) shows that the wedges were further separated and the stress changes in the rock were transmitted to the two auxiliary holes. At this time, the development of the tensile stress concentration zone was relatively small. The development of the compressive stress concentration area in zone E near the auxiliary holes is not as large as that in zone F, as shown by the circles of the upper and lower white elliptic curves. Tensile stress concentration occurs in the areas shown in A and B on the left and right sides of the auxiliary holes, which is equivalent to the degree of tensile stress concentration on the left and right sides of the circumference of the hole, i.e., part of the tensile stress acts on

the auxiliary holes. This concentration leads to the development path of rock fracture cracks, so from the results shown in Figure 13(b), it can change the direction and scope of the stress distribution and guide the crack development path. There is no tension stress concentration in the areas shown in C and D, but the area of the compression stress concentration in E of the lower part of the fracturing hole is much smaller than that in F of the upper part of the fracturing hole. This shows that no tensile stress concentration was observed in the C and D areas because the tension stress on the left and right inner ends of the auxiliary hole circumference is offset by the compression stress in E of the lower part of the crack hole.

Figure 14 shows the dynamic rock-breaking process induced by a hydraulic splitter with a 40° auxiliary hole.

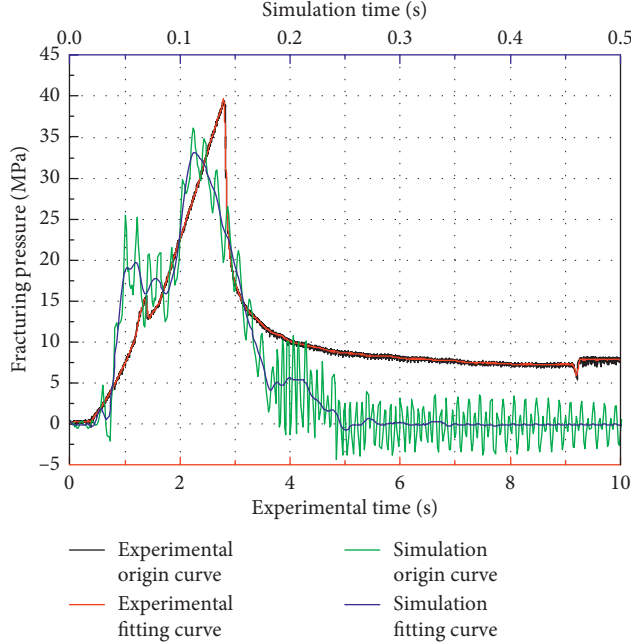


FIGURE 12: Numerical and experimental comparison of fracturing pressure at  $\alpha=40^\circ$ .

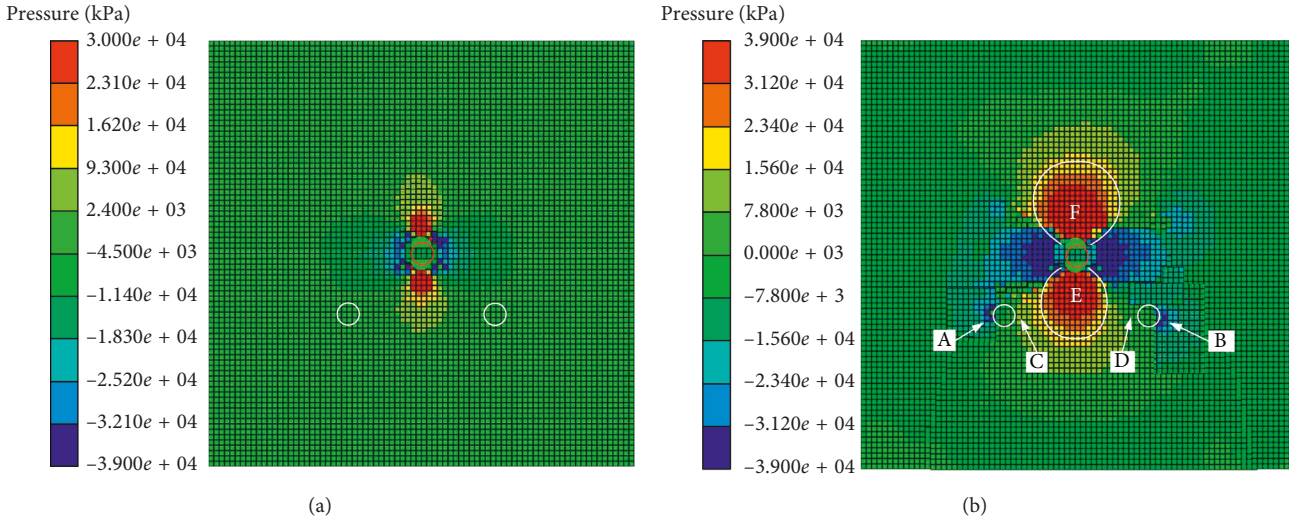


FIGURE 13: Equivalent effective stress nephogram of the auxiliary hole-assisted fracturing process at  $\alpha=40^\circ$ : (a) wedge contact predrilled fracturing hole; (b) stress concentration around auxiliary hole.

Figures 14(a)–14(d) are the crack initiation, crack propagation, crack crossing the auxiliary hole, and the fracture state of the rock, respectively.

As shown in Figure 14(a), the splitter wedge gradually contacts the borehole circumference at 0.14 s, and a compact crushing zone was formed around the borehole circumference. At 0.16 s, the crack extended to the position shown in Figure 14(b); the crack reaches the auxiliary hole and propagates in the directions of  $OO_1$  and  $OO_2$  near the cracking hole. As shown in Figure 14(c) at 0.2 s, the rock-breaking crack continues to break through the auxiliary holes, and the crack propagation is in a stagnant state at 0.04 s, indicating tensile stress after the crack reaches the auxiliary holes. When part of the stress is released

instantaneously, the residual stress is not enough to break the rock, so the wedge must continue separating a certain distance before the aggregated tensile stress can cause rock crack propagation. In addition, the dense zone in Figure 14(c) increases obviously, compared with Figure 14(b). When the crack in Figure 14(b) expands to the auxiliary hole, the tensile stress releases a part, but the compressive stress continues to squeeze the rock around the hole. Figure 14(d) shows the fracture state of the rock after failure, and two main cracks and two secondary cracks are present. Unlike the crack propagation in the rock without auxiliary holes, there is no main crack propagation in the upper half of the rock, far from the auxiliary holes. After passing through the auxiliary holes, the crack propagating

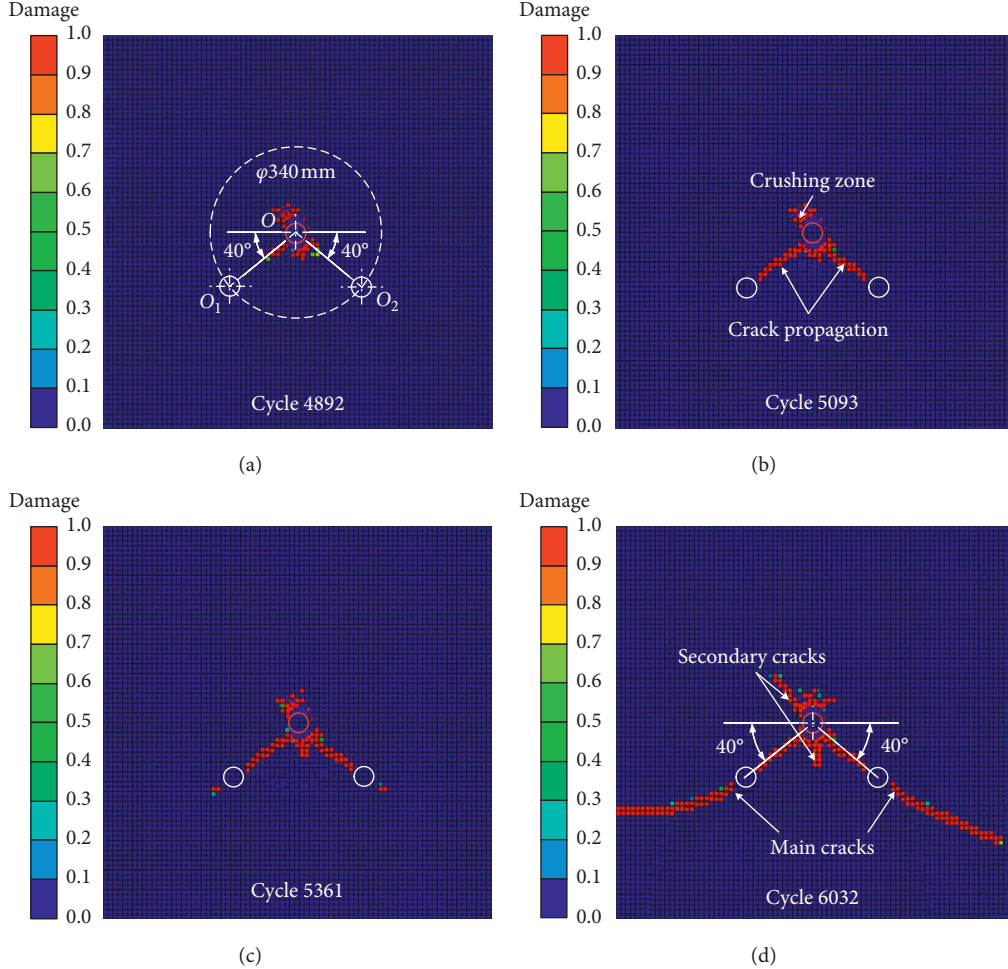


FIGURE 14: Dynamic rock-breaking process induced by a hydraulic splitter with a  $40^\circ$  auxiliary hole: (a) crushing zone formed; (b) crack reaches auxiliary hole; (c) crack crosses auxiliary hole; (d) rock fracture state.

direction gradually changes and no longer moves along the straight lines  $OO_1$  and  $OO_2$ ; however, it approaches horizontally and vertically to the side.

To study the effect of auxiliary holes on rock breaking, the crack propagation angle was also observed, as shown in Figure 14(d). It can be concluded that the crack propagates along the approximate straight lines  $OO_1$  and  $OO_2$  before extending to the auxiliary hole and then deflects to the horizontal straight line. The angle between the crack path and the horizontal straight-line direction of the two holes is approximately  $40^\circ$ . Therefore, the two holes can basically break the rock along the setting angle of the auxiliary holes, and the propagation path of the main crack is larger than that of the crack propagation angle diagram shown in Figure 11(b). The main crack now exists only on one side instead of both directions of wedge separation, and the angle between the crack propagation path and horizontal direction increases by approximately  $10^\circ$  under the same model settings and boundary condition. This result indicates that auxiliary holes can affect rock directional breaking.

As shown in Figure 15, the auxiliary holes with angles of  $\alpha = 45^\circ$  and  $50^\circ$  to the crack propagation were investigated. The crack propagation angles were  $40^\circ$  and  $42^\circ$ , respectively, at

$\alpha = 45^\circ$ , which is slightly less than the prefabricated angle of the auxiliary holes, and it can basically crush the rock along the setting angle of the auxiliary holes. When the prefabricated angle is  $50^\circ$ , the main crack in the crushed rock around the borehole no longer propagates along the straight lines  $OO_1$  and  $OO_2$ ; however, it deviates toward the horizontal direction. After the main crack passes over the auxiliary hole, the starting point of the main crack begins from the edge of the auxiliary empty hole. This shows that the auxiliary hole angle of  $50^\circ$  can no longer satisfy the induced rock-breaking effect.

The fracturing pressure variance with time with different prefabricated angles  $\alpha$  is shown in Figure 16. The fluctuation and stagnation of the fracturing pressure remain obvious in the process of rock breaking. These results show that the prefabricated angle  $\alpha = 45^\circ$  also plays an important role in the process of rock breaking. Figure 16 shows the curve of the swelling and cracking force when the hole is  $50^\circ$ . The fracturing pressure also fluctuates during the rock-breaking process at  $\alpha = 50^\circ$ , indicating that the crack passes through the auxiliary holes in the process of propagation. However, the peak value is significantly larger than that of  $40^\circ$  and  $45^\circ$ . From Figure 16(b), it can be observed that the percentage decrease of the fracturing pressure at  $\alpha = 50^\circ$  is lowest and the

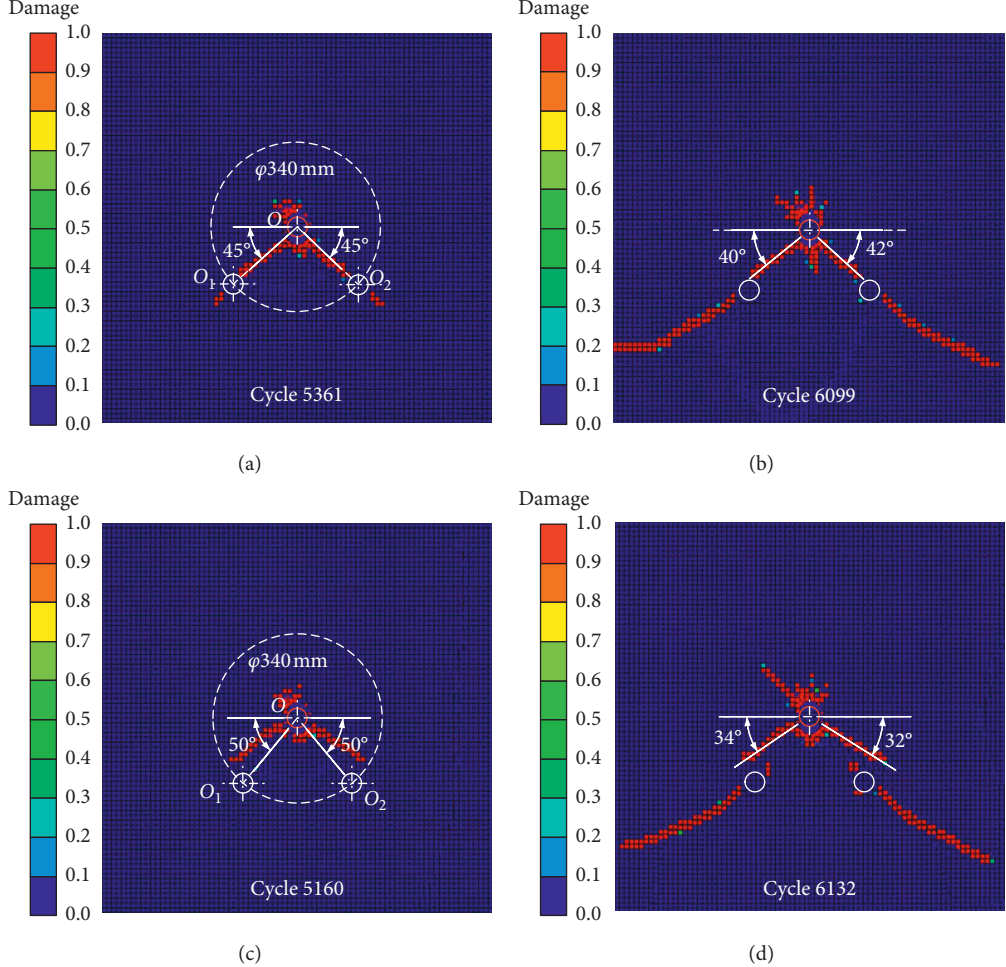


FIGURE 15: Dynamic rock-breaking process induced by a hydraulic splitter with different  $\alpha$ :  $\alpha = 45^\circ$  (a) at cycle 5361 and (b) at cycle 6099;  $\alpha = 50^\circ$  (c) at cycle 5160 and (d) at cycle 6132.

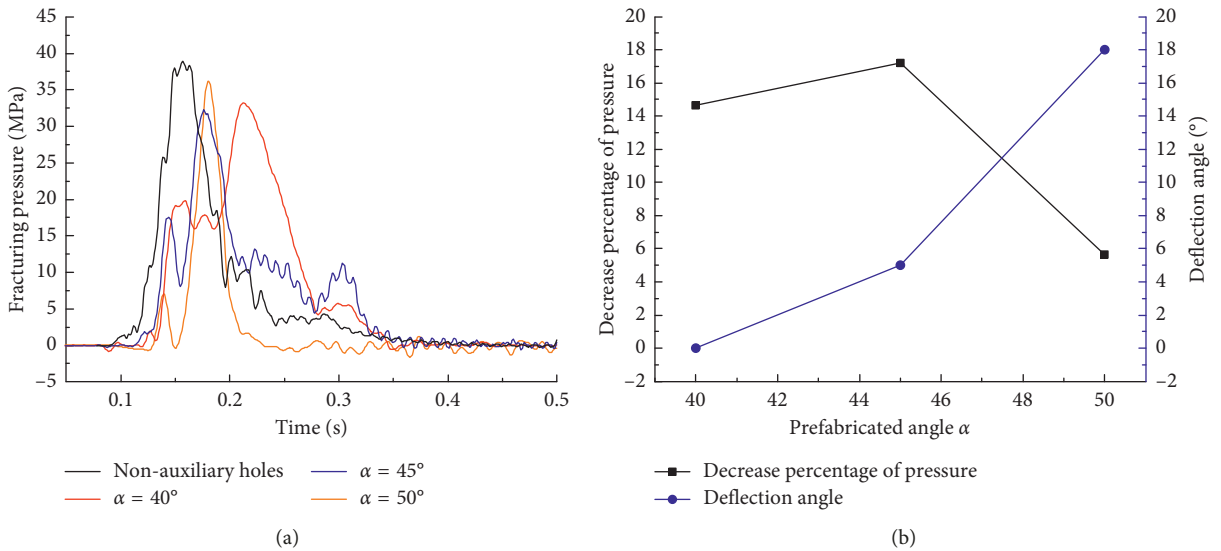


FIGURE 16: Graphs of data with different prefabricated angles  $\alpha$ : (a) variation principle of fracturing pressure with time; (b) decrease percentage of fracturing pressure and deflection angle changed with  $\alpha$ .

deflection angle (the difference value of the prefabricated angle and the crack propagation angle) is the largest, demonstrating that when the auxiliary holes are located at the prefabricated angles  $\alpha = 40^\circ$  and  $45^\circ$ , crack propagations can be well induced. However, the auxiliary holes cannot induce crack propagation in the process of rock breaking at  $\alpha = 50^\circ$ , but the fracturing pressure remains less than that with no auxiliary holes, indicating that the auxiliary holes play a positive role in guiding rock breaking.

## 6. Conclusions

In this work, a numerical model of rock breaking under hole assistance is established based on FEM coupling with SPH to reveal the rock-breaking mechanism and explain the reasons for crack formation and propagation under hole assistance. In addition, the numerical model was verified by experiment with and without hole. According to the numerical simulation and experimental results in the scope of this research, the following conclusions were made:

- (1) The simulation crack propagation angles without auxiliary holes were approximately  $30^\circ$ , appearing on the lower left and upper right parts, and the simulation results are basically consistent with the experimental results. In addition, the crack propagation angle and the fracturing pressure of the simulation assisted with auxiliary holes are in good agreement with those of the experiment, proving that the auxiliary holes play a guiding role in directional cracking. Both the experimental and simulation fracturing pressure under hole assistance show downward twists and turns in the upward trend, and the peak values of the fracturing pressure are 35.1 MPa and 39.9 MPa, respectively, with the 12% relative error.
- (2) The rock-breaking process by the hydraulic splitter under hole assistance is a process of energy dissipation. Two energy modes are mainly responsible for the rock breaking: the brittle failure energy consumed by tensile failure as well as the ductile failure energy consumed by shear and compressive failure. Unlike the crack propagation in the rock without auxiliary holes, there is no main crack propagation in the upper half of the rock, far from the auxiliary holes, and the cracks propagate along the approximate straight lines  $OO_1$  and  $OO_2$  before extending to the auxiliary hole. After passing through the auxiliary holes, the crack propagating direction gradually changes and no longer moves along the straight lines  $OO_1$  and  $OO_2$ ; however, it approaches horizontally and vertically to the side.
- (3) The results show that when the auxiliary holes are located at the prefabricated angles  $\alpha = 40^\circ$  and  $45^\circ$ , the crack propagation can be well induced and the cracks pass through the auxiliary holes. However, the auxiliary holes cannot well induce the crack propagation in the process of rock breaking at  $\alpha = 50^\circ$ , but the pressure is still less than that with no auxiliary holes, indicating that the auxiliary holes play a positive role in guiding rock breaking.

## Data Availability

The experimental and numerical data used to support the findings of this study are available from the corresponding author upon request.

## Conflicts of Interest

The authors declare that there are no conflicts of interest regarding the publication of this paper.

## Acknowledgments

This study was supported by the Fundamental Research Funds for the Central Universities (grant no. 2017XKZD02), the Top-Notch Academic Programs Project of Jiangsu Higher Education Institutions (TAPP), and the project funded by the Priority Academic Program Development of Jiangsu Higher Education Institutions (PAPD).

## References

- [1] Z. Xi-zeng, "Research and application of impact of broken rock type quick rock drivage line," *Coal Mine Machinery*, vol. 36, no. 3, pp. 188–190, 2015.
- [2] H. S. Li, S. Y. Liu, and P. P. Xu, "Numerical simulation on interaction stress analysis of rock with conical picks," *Tunnelling and Underground Space Technology*, vol. 85, pp. 231–242, 2019.
- [3] S. P. Singh, "Non-explosive applications of the PCF concept for underground excavation," *Tunnelling and Underground Space Technology*, vol. 13, no. 3, pp. 305–311, 1998.
- [4] E. Hoek and Z. T. Bieniawski, "Brittle fracture propagation in rock under compression," *International Journal of Fracture*, vol. 26, no. 4, pp. 276–294, 1984.
- [5] W. F. Brace, B. W. Paulding, and C. Scholz, "Dilatancy in the fracture of crystalline rocks," *Journal of Geophysical Research*, vol. 71, no. 16, pp. 3939–3953, 1966.
- [6] P. Z. Bazant and L. Cedolin, "Blunt-crack band propagation in finite-element analysis for concrete structures," *Journal of the Engineering Mechanics Division*, vol. 105, pp. 297–315, 1983.
- [7] G. Han, M. Bruno, and M. B. Dusseault, "Dynamically modelling rock failure in percussion drilling," in *Proceedings of the 40th U.S. Symposium on Rock Mechanics*, American Rock Mechanics Association, Anchorage, Alaska, USA, June 2005.
- [8] G. Han, M. Bruno, and T. Grant, "Lab investigations of percussion drilling: from single impact to full scale fluid hammer," in *Proceedings of the 41st U.S. Rock Mechanics Symposium*, American Rock Mechanics Association, Golden, CO, USA, June 2006.
- [9] M. M. Hossain, M. K. Rahman, and S. S. Rahman, "Hydraulic fracture initiation and propagation: roles of wellbore trajectory, perforation and stress regimes," *Journal of Petroleum Science and Engineering*, vol. 27, no. 3-4, pp. 129–149, 2000.
- [10] H. Zhu, J. Deng, X. Jin, L. Hu, and B. Luo, "Hydraulic fracture initiation and propagation from wellbore with oriented perforation," *Rock Mechanics and Rock Engineering*, vol. 48, no. 2, pp. 585–601, 2015.
- [11] Z. Guangqing and C. Mian, "Complex fracture shapes in hydraulic fracturing with orientated perforations," *Petroleum Exploration and Development*, vol. 36, no. 1, pp. 103–107, 2009.

- [12] W. Peng, M. Xian-biao, L. Jin-bin, and D. Chun-zhi, "Study of the borehole hydraulic fracturing and the principle of gas seepage in the coal seam," *Procedia Earth and Planetary Science*, vol. 1, no. 1, pp. 1561–1573, 2009.
- [13] L. Zhi-long, Z. Jin-Zhang, W. Xiu-xi, W. Hen-gan, and X. Bing, "Simulation study on characteristics of hydraulic fracturing propagation," *Rock and Soil Mechanics*, vol. 30, no. 1, pp. 169–174, 2009.
- [14] F. Hamidi and A. Mortazavi, "A new three dimensional approach to numerically model hydraulic fracturing process," *Journal of Petroleum Science and Engineering*, vol. 124, pp. 451–467, 2014.
- [15] J. Kim and G. J. Moridis, "Numerical analysis of fracture propagation during hydraulic fracturing operations in shale gas systems," *International Journal of Rock Mechanics and Mining Sciences*, vol. 76, pp. 127–137, 2015.
- [16] A. R. Ingraffea and F. E. Heuze, "Finite element models for rock fracture mechanics," *International Journal for Numerical and Analytical Methods in Geomechanics*, vol. 4, no. 1, pp. 25–43, 2010.
- [17] H. Zhu, J. Guo, X. Zhao, Q. Lu, B. Luo, and Y.-C. Feng, "Hydraulic fracture initiation pressure of anisotropic shale gas reservoirs," *Geomechanics and Engineering*, vol. 7, no. 4, pp. 403–430, 2014.
- [18] H.-Y. Zhu, J.-G. Deng, Y.-H. Xie, K.-W. Huang, J.-Y. Zhao, and B.-H. Yu, "Rock mechanics characteristic of complex formation and faster drilling techniques in western south China sea oilfields," *Ocean Engineering*, vol. 44, pp. 33–45, 2012.
- [19] H. Zhu, C. Zhang, J. Deng et al., "Characteristics of rock mechanics and PDC bit optimization of glutenite formation in the Pearl River Mouth Basin oil fields," *Scientia Iranica*, vol. 20, no. 4, pp. 1133–1144, 2013.
- [20] T. Ito and K. Hayashi, "Analysis of crack reopening behavior for hydrofrac stress measurement," *International Journal of Rock Mechanics and Mining Sciences & Geomechanics Abstracts*, vol. 30, no. 7, pp. 1235–1240, 1993.
- [21] H. Horii and S. Nemat-Nasser, "Compression-induced microcrack growth in brittle solids: axial splitting and shear failure," *Journal of Geophysical Research Solid Earth*, vol. 90, no. 4, pp. 3105–3125, 1985.
- [22] E. Komurlu and A. Kesimal, "Evaluation of indirect tensile strength of rocks using different types of jaws," *Rock Mechanics and Rock Engineering*, vol. 48, no. 4, pp. 1723–1730, 2015.
- [23] R. Chen and B. Stimpson, "Interpretation of indirect tensile strength tests when moduli of deformation in compression and in tension are different," *Rock Mechanics and Rock Engineering*, vol. 26, no. 2, pp. 183–189, 1993.
- [24] P. J. Van Den Hoek, J. T. M. Van Den Berg, and J. Shlyapobersky, "Theoretical and experimental investigation of rock dilatancy near the tip of a propagating hydraulic fracture," *International Journal of Rock Mechanics and Mining Sciences & Geomechanics Abstracts*, vol. 30, no. 7, pp. 1261–1264, 1993.
- [25] L. N. Germanovich and A. V. Dyskin, "Fracture mechanisms and instability of openings in compression," *International Journal of Rock Mechanics and Mining Sciences*, vol. 37, no. 1-2, pp. 263–284, 2000.
- [26] E. J. Sellers and P. Klerck, "Modelling of the effect of discontinuities on the extent of the fracture zone surrounding deep tunnels," *Tunnelling and Underground Space Technology*, vol. 15, no. 4, pp. 463–469, 2000.
- [27] H. Y. Zhu, J. G. Deng, S. J. Liu et al., "Hydraulic fracturing experiments of highly deviated well with oriented perforation technique," *Geomechanics and Engineering*, vol. 6, no. 2, pp. 153–172, 2014.
- [28] H.-Y. Zhu, L. Tao, Q.-Y. Liu, Z.-D. Lei, S. Jiang, and J. D. McLennan, "Fracture characteristics and change of permeability under the influence of natural fractures: experimental study of Wufeng-Longmaxi shale," *SPE Reservoir Evaluation & Engineering*, vol. 21, no. 2, pp. 225–237, 2018.
- [29] J. Gu and Z. Zhao, "Considerations of the discontinuous deformation analysis on wave propagation problems," *International Journal for Numerical and Analytical Methods in Geomechanics*, vol. 33, no. 12, pp. 1449–1465, 2010.
- [30] Z. Hao, C. Zhou, B. Lin, Y. Pang, and Z. Li, "Pressure-relief and permeability-increase technology of high liquid-solid coupling blast and its application," *International Journal of Mining Science and Technology*, vol. 24, no. 1, pp. 45–49, 2014.
- [31] M. Grujicic and W. C. Bell, "Smart-fuze design and development based on computational analysis of Warhead/urban-target interactions," *Researches and Applications in Mechanical Engineering*, vol. 2, no. 1, pp. 1–10, 2013.
- [32] G. R. Johnson and T. J. Holmquist, "Response of boron carbide subjected to large strains, high strain rates, and high pressures," *Journal of Applied Physics*, vol. 85, no. 12, pp. 8060–8073, 1999.
- [33] H. A. Ai and T. J. Ahrens, "Simulation of dynamic response of granite: a numerical approach of shock-induced damage beneath impact craters," *International Journal of Impact Engineering*, vol. 33, no. 1–12, pp. 1–10, 2006.
- [34] X. Zhang, H. Hao, and G. Ma, "Dynamic material model of annealed soda-lime glass," *International Journal of Impact Engineering*, vol. 77, pp. 108–119, 2015.
- [35] M. A. Iqbal, A. Rajput, and N. K. Gupta, "Performance of pre-stressed concrete targets against projectile impact," *International Journal of Impact Engineering*, vol. 110, pp. 15–25, 2017.
- [36] M. M. Dehghan Banadaki and B. Mohanty, "Numerical simulation of stress wave induced fractures in rock," *International Journal of Impact Engineering*, vol. 40–41, no. 2, pp. 16–25, 2012.
- [37] F. Xiao-Wei, L. Jun-Cheng, W. Hong-Bo, and C. Jing-Zhen, "Mesomechanism of elastic precursor decay in alumina under plate impact loading," *Acta Physica Sinica*, vol. 65, no. 16, Article ID 166201, 2016.

